CLAS-ANALYSIS 2007-117

Search for $\Phi^{--}(1862)$ Pentaquark State in $\Xi^-\pi^-$ Decay Channel Using EG3 Data

H. Egiyan, M. Holtrop, E. Smith, S. Stepanyan, R. Gothe, J. Langheinrich, M. Ito, G. Mutchler, Zh. Zhao, P. Mattione

November 11, 2007

Abstract

We analyze the entire EG3 data set searching for the $\Phi^{--}(1862)$ pentaquark in the $\Xi^-\pi^-$ decay channel using CLAS. The invariant mass spectra of $\Lambda\pi^-\pi^-$ and $\Xi^-\pi^-$ systems do not show any statistically significant enhancement near mass $M = 1.860$ `GeV`. The statistical analysis of the sideband-subtracted mass spectrum yields an upper limit of 200 `pb` for the photoproduction cross section of $\Phi^{--}(1862)$ with a subsequent decay to $\Xi^-\pi^-$ system in the photon energy range 4.5 `GeV` $< E_\gamma <$ 5.5 `GeV`.

Contents

1 Introduction **3**

2 Experimental Data from CLAS **3**

3 Data Reduction and Processing **5**

4 Identification of $\Lambda(1116)$ **5**

5 Identification of negative pions **7**

6 Energy Loss Correction **8**

7 Momentum Corrections **9**

8 Selection of $\Xi^-(1321)$ events **10**
8.1 Liberal Selection of Events 10
8.2 Conservative Selection of Events 12

9 Fiducial and Energy Cuts **12**

10 Acceptance **16**
10.1 Definition 16
10.2 Simulations 18
10.3 Model Dependence 19

11 Normalization **22**

12 Systematics **23**

13 Invariant mass spectrum for $\Lambda\pi^-\pi^-$ system **24**

14 Invariant mass spectrum for $\Xi^-\pi^-$ system **25**
14.1 Sideband Subtraction 25
14.2 Cross-check with Fitting method 26

15 Upper Limits **26**
15.1 Methods to estimate the upper limits 28
15.1.1 Rolke Method with Poisson Statistics 28

15.1.2 Rolke Method with Gaussian Statistics 30
15.1.3 Feldman-Cousins method 30
15.2 Upper limits for cross sections 31

16 Conclusions **32**

A Appendix **33**
A.1 Good Runs 33

1 Introduction

During last five years there has been a number of experimental observations, including from CLAS, of a narrow exotic S=+1 baryon state at a mass of approximately 1.54 GeV. These observations, if true, would confirm the existence of the Θ^+, which is the predicted spin 1/2, isospin 0, member of the anti-decuplet of baryons within the Chiral Soliton Model [1]. The anti-decuplet (see Fig. 1) contains three explicitly exotic states located at the apexes whose quantum numbers require a minimal quark content of four quarks and one anti-quark. These exotic states cannot be accommodated within the simple quark model which assumes all baryons are built out of 3 quarks. On the other hand, there has been a number of other high statistics experiments which tried to search for the Θ^+ signal but failed to observe any statistically significant enhancement near 1.54 GeV. The existence of the Θ^+ is still considered as an open question.

Besides the $\Theta^+(1540)$, the other exotic states have $S = -2$ and charge $Q = -2$ and $Q = +1$, which we willdenote by Φ^{--} and Φ^+ respectively. These exotic cascade states have isospin 3/2. Two additional partners, denoted Φ^- and Φ^0, are also pentaquark states but are not explicitly exotic. The NA49 collaboration has reported evidence for the strangeness $S = -2$ pentaquark Φ^{--} and the Φ^0 at a mass of 1.862 GeV [2]. The states were reconstructed from their decay products using their decays into $\Phi^{--} \to \Xi^-\pi^-$ and $\Phi^0 \to \Xi^-\pi^+$. These observations are critical for verifying the existence of the anti-decuplet of pentaquarks, and require confirmation. We also note that many experiments [3, 4, 5, 6, 7, 8, 9, 10, 11, 12, 13], some of which represented a much larger statistical sample, have not been able to confirm this observation.

The purpose of this analysis is to search specifically for the $\Phi^{--}(1862)$ of the anti-decuplet with the CLAS detector [14] in a photoproduction experiment. This paper will review the EG3 data analysis performed to look for an evidence for existence of any signal in the $\Xi^-(1321)\pi^-$ decay channel.

2 Experimental Data from CLAS

The eg3 data was collected in December of 2004 and January of 2005, dividing the run into two segments, which we will refer to as before Christmas and after Christmas, respectively. The detector configuration was chosen to satisfy

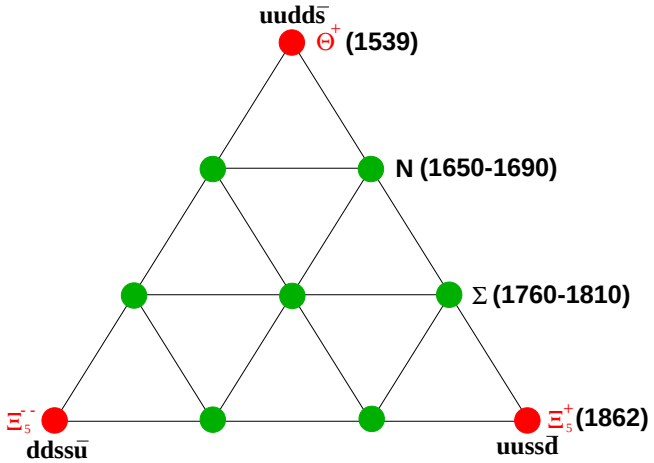

Figure 1: Anti-decuplet predicted by the chiral soliton model [15]. The masses in parenthesis are updated values for the predicted masses. The red corners of the anti-decuplet have exotic quantum numbers. The quark content of the exotic members are also displayed.

the specification described in the experimental proposal [16]. The electron beam energy averaged from the reported by the Hall A and C arc measurements was 5765.5 MeV and 5768.3 MeV before and after Christmas, respectively. The electron beam passed through a radiator with a nominal thickness of 5×10^{-4} r.l. and was bent into the CLAS tagging system, were the electron energy was measured. The photon beam from the radiator impinged upon a 40 cm long and 4 cm wide liquid deuterium target positioned 50 cm upstream of the nominal CLAS target position. The standard electron beam current was chosen to be 30 nA, and it was limited by the drift chamber performance. There were two Level 1 trigger configurations selected as trigger bits five and six. Trigger bit five was set as a two track trigger requiring a coincidence in the TOF system and start counter in the same sector in at least two sectors: $(TOF \times ST)^2$. Trigger bit six was a three track trigger requiring either TOF and ST coincidence in at least three sectors, or TOF and ST coincidence in two sectors, but one of the sectors having at least two start counter paddles being hit: $[(TOF \times ST)^3] \oplus [(TOF \times ST) \times (TOF \times ST \times ST)]$. The bit 5 trigger was prescaled with a factor which varied from run to run to allow for less than 20% deadtime. This experiment did not use the Level 2 trigger capability of CLAS.

3 Data Reduction and Processing

The raw data from the CLAS detector were recorded on the tapes of the Jefferson Lab tape silo in BOS format files [17]. After the calibration of all subsystems was finished, these files were retrieved from the silo and processed using the off-line event reconstruction code. For each raw data file a single job was launched on the Jefferson Lab Linux batch farm. For each job a raw data file was analyzed and an output ("cooked") BOS file was produced. Then a sequence of filtering programs, selecting a significantly reduced data sample, were run on the output files to produce filtered BOS files, which contained the same BOS banks [17] but for far fewer number of events. These kinds of filtering (or skimming) procedures are effective for reactions with relatively small cross sections, such as processes involving production of strange particles. In addition, ROOT [18] files, containing ROOT trees, were produced from the cooked and filtered files. The ROOT files are relatively smaller in size than the BOS files, and they contain information from only the essential for analyses BOS banks. This makes them more convenient for a higher level analysis, involving a smaller subset of total events. The runs used in this analysis are given in Appendix A.1. The current analysis described in this paper was done using skimmed ROOT files containing at least one candidate for $\Lambda(1116)$.

4 Identification of $\Lambda(1116)$

The first step for the event selection chain for this analysis is identification of the $\Lambda(1116)$ charged decay products - a proton and a π^-. The files from Λ-skim are already preselected to contain only events with at least one Λ candidate pair, which is one positive and one negative time based tracks with invariant mass restrictions :

$$(|M_c - 1.1157\ \texttt{GeV}| < 0.017\ \texttt{GeV}) \oplus (|M_u - 1.1150\ \texttt{GeV}| < 0.017\ \texttt{GeV}), \quad (1)$$

where M_c and M_u are corrected and uncorrected for energy loss invariant masses of the pair. The invariant masses are calculated by assuming that the negative particle in a pair is a π^-, and the positive particle is a proton. The effects of the energy loss corrections are described in Section 6. No other cuts were used during filtering Λ-skim files.

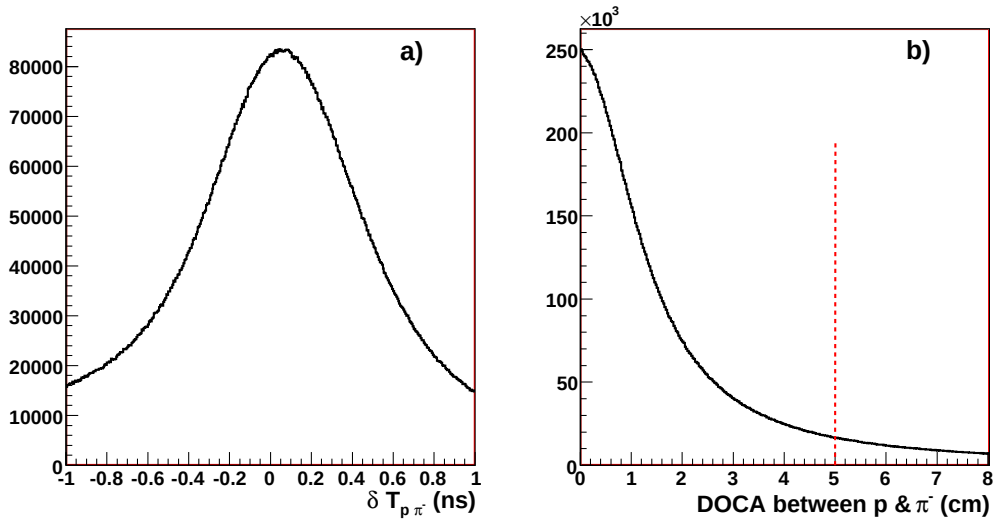

Figure 2: The time difference between proton and π^- (a), and the DOCA distribution between proton and π^- tracks (b).

In the offline analysis additional requirements are applied to select proton and π^- from Λ-decays. In this procedure we consider all possible pairings of negative and positive tracks, similar to what is done during skimming. For each pair we assume that the negative particle in a pair is a π^-, and the positive particle is a proton. First we require that the vertex times of the proton and π^- be within ± 1 ns from each other. The vertex time difference between protons and negative pions is shown in Fig. 2 a. The resolution for the vertex time difference is ~ 300 ps. Because the decay products originate from the same point in space, a 5 cm cut is applied on the Distance-Of-Closest-Approach (DOCA). DOCA is defined as the shortest line segment connecting straight lines defined by track momentum and vertex information from the EVNT bank. DOCA distribution is shown in Fig. 2 b. The invariant mass cut applied in the offline analysis is 1.1120 GeV$< M_{p\pi^-} <$ 1.1206 GeV[1]. If there are more than one $p-\pi^-$ pairs satisfying this criteria the best pair is selected which yields the minimal value for quantity χ^2_Λ defined as:

$$\chi^2_\Lambda = \left(\frac{M_{p\pi^-} - M_\Lambda}{0.0017\ \texttt{GeV}}\right)^2 + \left(\frac{T_p - T_{\pi^-}}{0.45\ \texttt{ns}}\right)^2 + \left(\frac{DOCA(p\pi^-)}{1.5\ \texttt{cm}}\right)^2, \qquad (2)$$

[1]The cut is actually applied on the invariant mass of the pair after the energy loss and momentum corrections are applied.

where M_I is the invariant mass of the pair, T_p and T_{π^-} are vertex times of proton and π^-.

5 Identification of negative pions

After we found the $\Lambda(1116)$ decay products using the procedure described in Section 4 we can assume with more certainty that the negative particle in the pair is a π^-, and use this hypothesis to verify the start time of the event. The standard SEB package does determine the event start time based on the vertex times of all the tracks in the event, also taking into account the offset of the event interaction with respect to the center of the target. The SEB procedure attempts to find the right RF bucket associated with the electron beam bunch by matching the tagger RF time with the vertex time reconstructed by the CLAS. Due to the large number of the hits in the tagger at the EG3 running condition this matching is not always correct. For that reason we use the vertex time of the π^- from the Λ-decay instead of a photon from the tagger hodoscope to reselect the RF bunch. Note that the RF signal does not have to be present in the data stream since the SEB start time is already determined from the photon time in the tagger, and the photon time in the tagger is very closely correlated with the RF bucket time within 200 ps.

We offset the start time of the event contained in the HEVT bank by a multiple of 2.004 ns required by the vertex time of the π^-. The vertex time is defined as the pion vertex time. This time is not propagated to the target center; instead, it is directly compared with the start time given in the HEVT bank, and the required time offset multiple of 2.004 ns is obtained:

$$T_0^{new} = T_0^{SEB} - 2.004 \texttt{ ns } R\left(\frac{T_0^{SEB} - T_{\pi^-}}{2.004 \texttt{ ns}}\right), \tag{3}$$

where T_0^{new} is the new adjusted start time for the event, T_0^{SEB} is the original event start time from the HEVT bank, T_{π^-} is the vertex time of the negative pion, and the 2.004 ns is the bunch separation time for the Hall B electron beam. R stands for rounding up to the nearest integer number. A comparison of the velocity β of the negative tracks determined from the time-of-flight system of CLAS versus their momentum before and after adjustment of the event start time is shown in Fig. 3, panels a and b respectively. One can clearly see that the start time adjustment procedure significantly reduced

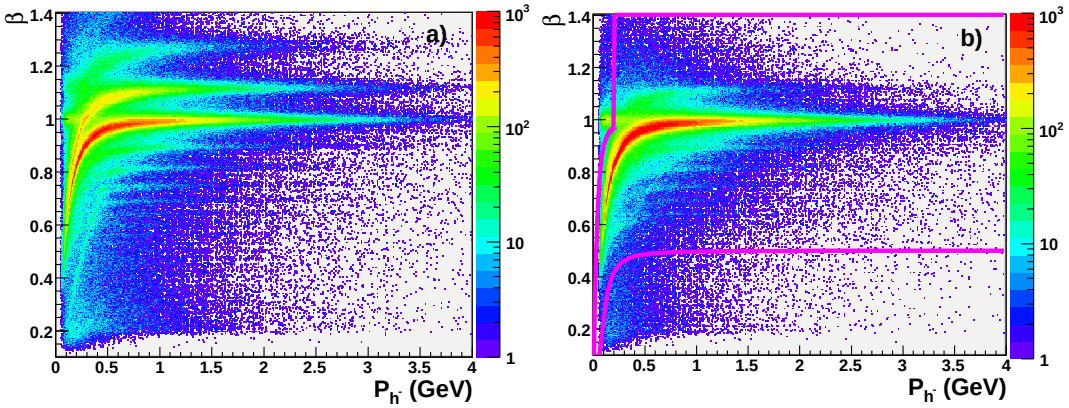

Figure 3: Plots of β from SEB (a) and β with adjusted start time (b) versus momentum of negative tracks from Λ skim files. The magenta curves in the left panel indicate the boundaries of the π^- selection area.

the whisker-like structures due to RF bucket misidentification when a wrong photon is selected in the tagger. Once the event start time is determined, the negative pions are identified by comparing imposing cuts on the β versus momentum plot as illustrated by magenta curves in Fig. 3 b.

6 Energy Loss Correction

When particles from the photon-target interaction pass through the material in the target region of CLAS they may lose part of the energy due to ionization. The amount of the energy loss depends on the charge and the velocity of the particle, and the type and amount of the material it traverses. In order to account for these effects energy loss corrections were applied according to *eloss* procedure [20]. A comparison of the $\Lambda(1116)$ mass before and after energy loss corrections is shown in Fig. 4. The peak becomes more narrow $\sigma_\Lambda \sim 1.5$ MeV, and the location of the peak becomes more consistent with the PDG value of $M_\Lambda = 1.115683$ GeV. Most of the improvement comes from the corrections for the negative pions from $\Lambda(1116)$ decays that have energy typically less than 500 MeV. The average mass resolution of the $p\pi^-$ system in this data sample is about 1.6 MeV. The energy loss corrections are applied to all particles involved in this analysis.

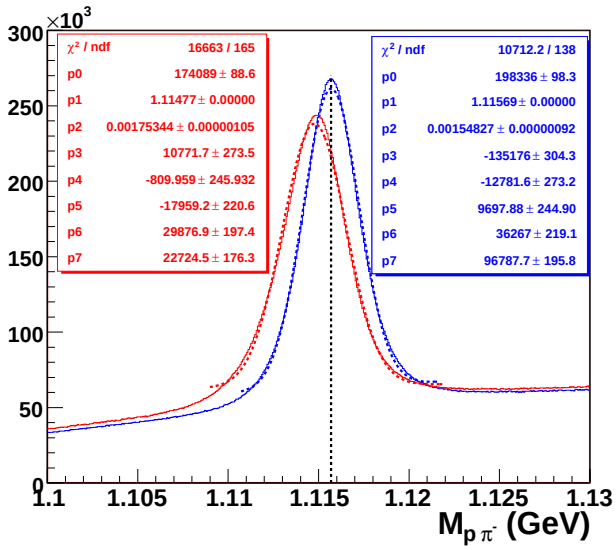

Figure 4: Mass spectrum of the $p\pi^-$ system before (red) and after (blue) energy loss corrections are applied. The dashed vertical line shows the PDG [19] value for the mass of $\Lambda(1116)$.

7 Momentum Corrections

Even after energy loss corrections are performed, there systematic uncertainties still remainsin the particle momentum determined from CLAS using the standard reconstruction software. These uncertainties can be due to the misalignment of the torus magnet cryostats with respect to the CLAS drift chambers, energy loss of particles in the drift chamber region not accounted for in the *eloss* package [20], or software or calibration shortcomings. These errors in the momentum determination can lead to shifts of the masses of decayed or missing particles and widening of the peaks. A procedure was developed to determined the necessary momentum correction based on kinematic fitting [21].The resulting momentum corrections were small, and their application does not change the main conclusions of this analysis.

8 Selection of $\Xi^-(1321)$ events

After selecting the best candidate pair for $\Lambda(1116)$ we proceed with combining it with the remaining negative pions in the event. For further analysis we require that an event contained at least two more negative pions in addition to the π^- in the $\Lambda(1116)$-pair. Therefore one can have multiple combinations of pairings ($\Lambda\pi^-$). One either can use all combinations, or, alternatively, one could select the pair which is most consistent with a ground state cascade $\Xi(1321)$ based on the vertex information and the invariant mass. The former yields worse signal-to-background ratio, while the latter, although provides better signal-to-background ratio, can distort the content of the sidebands around the cascade peak. We tried both approaches in our analysis, and they are described in the subsection below.

8.1 Liberal Selection of Events

First we attempt to obtain an event ensemble which provides a very good signal-to-background ratio with little concern about quality of the events. This means that we neither select the best runs, nor do we apply fiducial cuts or matching between a photon in the tagger and the event detected in CLAS. For each event we only select one $\pi^-\Lambda$ pair for which the common vertex and the invariant mass are most consistent with a decaying ground cascade. The selection criteria is to minimize the following quantity:

$$\chi^2_\Xi = \left(\frac{M_{\Lambda\pi^-} - M_\Xi}{2.1\ \texttt{MeV}}\right)^2 + \left(\frac{DOCA(\Lambda\pi^-)}{2.25\ \texttt{cm}}\right)^2 \tag{4}$$

With this kind of selection of events we merely try to see if we can see any enhancement in the $\Lambda(1116)\pi^-\pi^-$ invariant mass. A two dimensional plot showing the proper time $c\tau$ of the assumed $\Xi^-(1321)$ versus the invariant mass of $\Lambda\pi^-$ system is shown on Fig. 5. The cascade ground $\Xi(1321)$ weakly decays into $\Lambda\pi$, and has a width negligible compared to the CLAS energy resolution, while the $\Sigma^-(1385)$ decays into $\Lambda\pi$ through strong interaction with a relatively large width of 39.4 MeV [19], creating a significant background to $\Xi(1321)$ events. A vertical band corresponding to $\Xi^-(1321)$ extends to quite large values of $c\tau$, therefore providing an additional handle for enhancing the signal-to-background ratio. After applying a cut $c\tau > 1.5$ cm we get a relatively clean $\Xi^-(1321)$ peak containing $\sim$ 1700 events with signal-to-background ratio of ~ 0.8 (see Fig. 6 a).

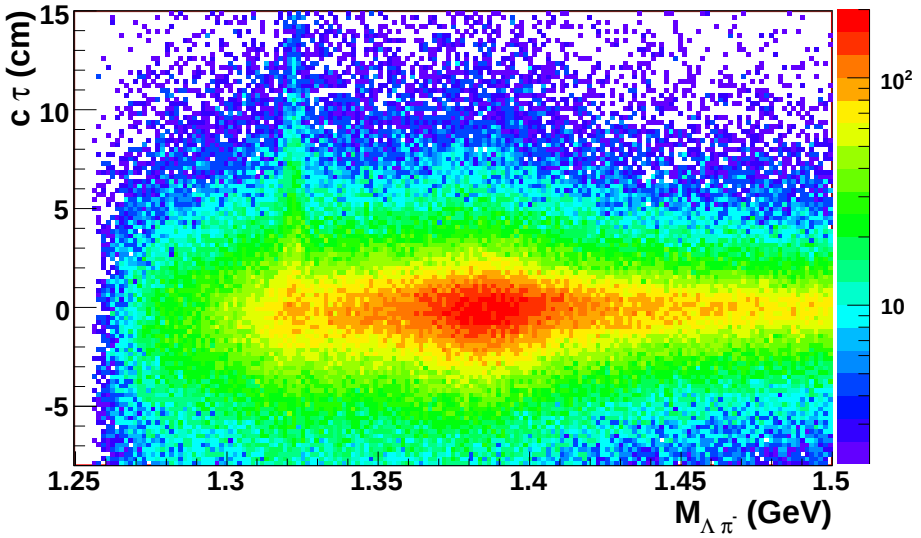

Figure 5: Distribution of $c\tau$ versus invariant mass of $\Lambda\pi^-$ system with "liberal selection". The vertical band corresponding to $\Xi^-(1321)$ extends to larger values of $c\tau$ providing an extra handle for selecting desired events.

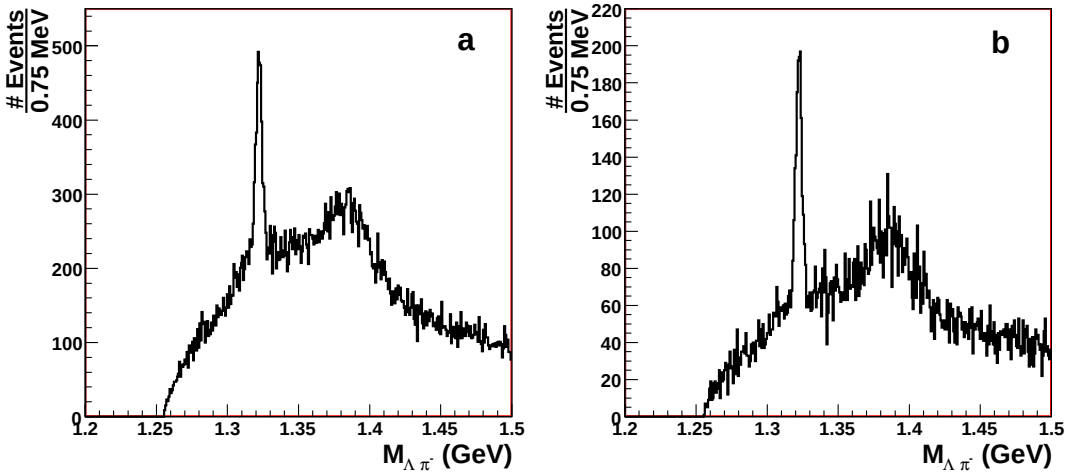

Figure 6: Invariant mass distribution of $\Lambda\pi^-$ system with "liberal selection" with an extra lifetime cut $c\tau > 1.5$ cm for $\Lambda\pi^-\pi^-$ events (a) and $K^+\Lambda\pi^-\pi^-$ events (b).

In fact we can even improve the signal-to-background ratio by requiring an additional K^+ in the event. This reduces the number of events by a factor of two. The invariant mass of $\Lambda(1116)\pi^-$ system with an additional kaon is shown in Fig. 6 b.

8.2 Conservative Selection of Events

If one wants to obtain absolute cross sections with CLAS then one needs to select only events from the runs which did not have significant hardware problems, use only tracks in the fiducial regions of CLAS, and also be able to match the event with one of the tagger E-counters. In our case the possible photon range should be within the tagger Master OR (MOR) range used in coincidence with Level 1 trigger. In addition, if one would like to extract the number of the events containing $\Xi^-(1321)$ using sideband subtraction or fitting, then selecting only the "best" $\pi^-\Lambda$ will distort the shape of the background resulting in a more ragged structure underneath and around the $\Xi^-(1321)$ mass peak. Therefore, all possible combinations of $\Lambda\pi^-$ are included in the invariant mass spectrum of $\Lambda\pi^-$ system. The mass distribution shown in Fig. 7 features two very distinct structures: first is a narrow structure near $M = 1.321$ GeV corresponding to $\Xi(1321)$, and the second one is a broader structure center at $M =$ 1.385 `GeV` corresponding to $\Sigma^-(1385)$. This selection does not distort the backround, and we can apply the sideband subtraction method to obtain the $\Xi(1321)\pi^-$ mass spectrum. But these selection of events drastically reduces the number of events in the cascade peak.

9 Fiducial and Energy Cuts

There were two additional kinds of cuts in this analysis applied to both the real data and the Monte Carlo (MC) simulations. The first kind are the geometrical fiducial cuts, applied in order to select the regions of the relatively uniform detector response which could also could be reproduced by the *GSIM* simulation program. These cuts select angular ranges in the laboratory frame for various values of 3-momentum of positive and negative particles. Sample plots of these cuts for π^- are shown in Fig. 8, and for protons are shown in Fig. 9. The blue areas are the accepted events, the red areas are rejected events.

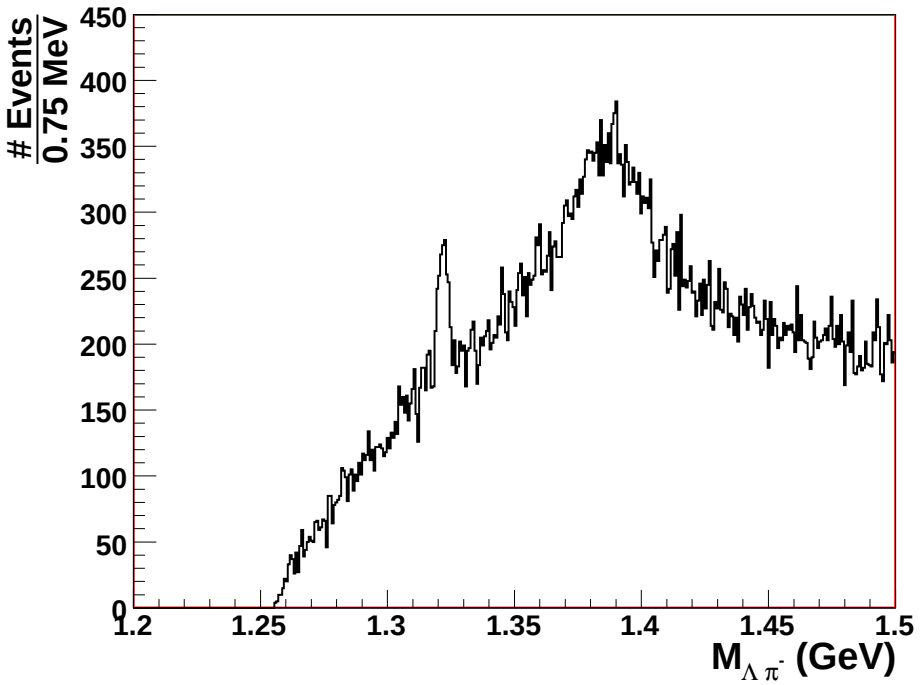

Figure 7: Invariant mass distribution of $\Lambda\pi^-$ system with "conservative selection" with $c\tau > 0$ cm for $\Lambda\pi^-\pi^-$ events.

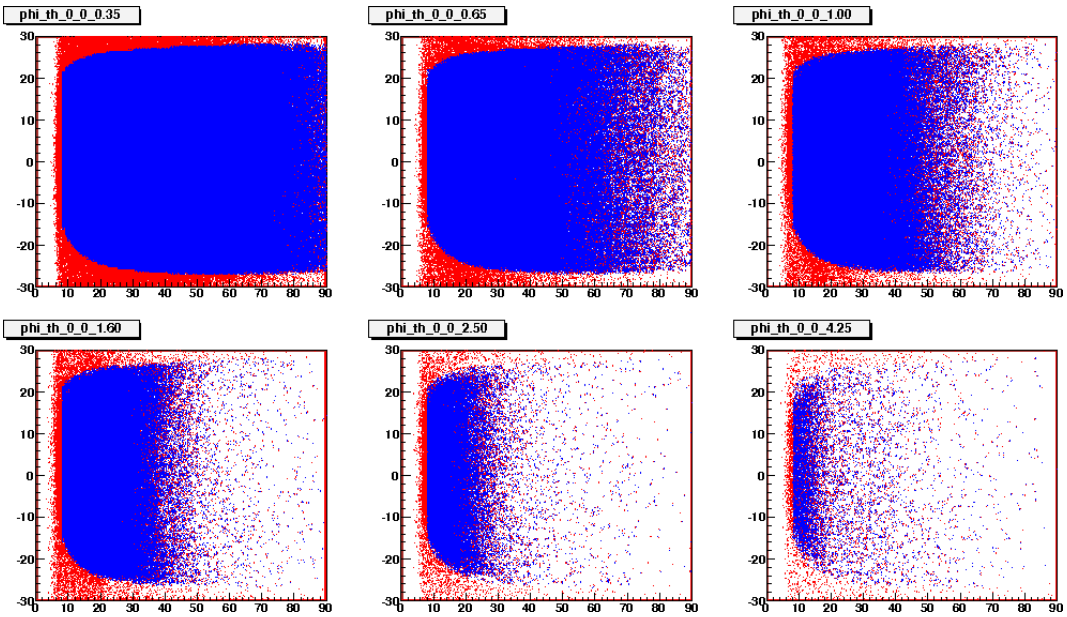

Figure 8: Laboratory angles ϕ versus θ for negative tracks in Sector 1 for various momentum ranges. The red areas are rejected regions, the blue areas are the accepted regions.

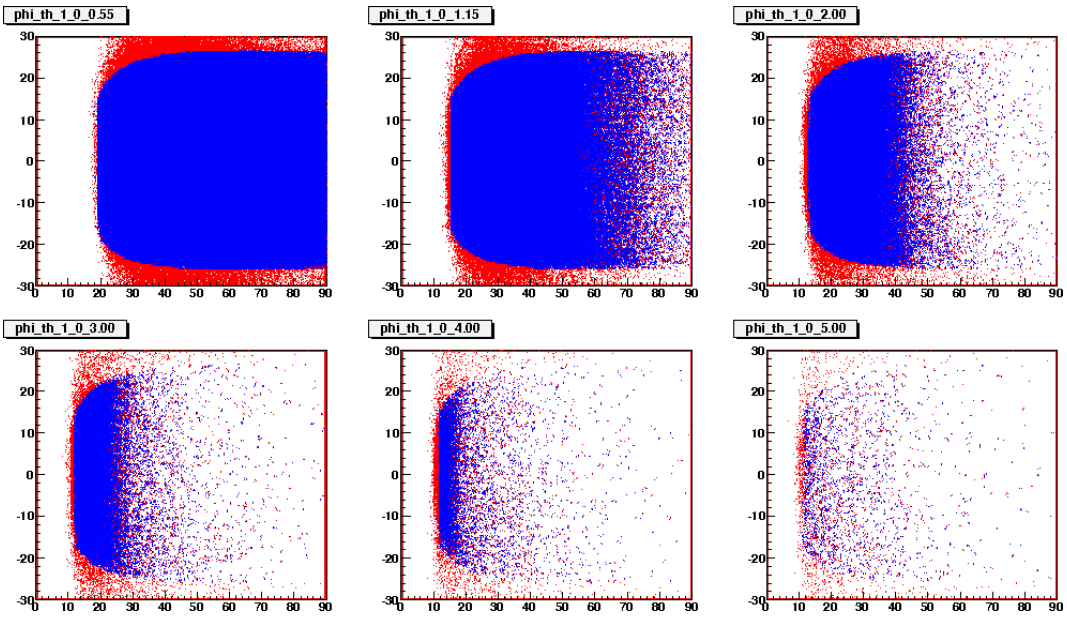

Figure 9: Laboratory angles ϕ versus θ for positive tracks in Sector 1 for various momentum ranges. The red areas are rejected regions, the blue areas are the accepted regions.

The second kind are the kinematic cuts which can be imposed on the kinematic quantities to enhance the signal. In this analysis we can impose such a cut on the missing mass of the remaining system after $\Xi(1321)^-\pi^-$ system is identified. To conserve strangeness in the strong and electromagnetic interactions leading to cascade photoproduction we can expect two addition kaons to be produced on deuteron. This can be utilized by requiring at least one tagger hit matching in time and satisfying the missing mass contraint:

$$M_{miss} = \sqrt{[(p_\gamma + p_d) - (p_{\Xi^-} + p_{\pi^-})]^2} > 2M_{K^+}, \tag{5}$$

where p_γ, p_d, p_{Ξ^-}, and p_{π^-} are 4-vectors for the photon, deuteron, $\Xi(1321)^-$, and π^- respectively. Only tagger hits with status word in the TAGR bank equal to 7 or 15 were used, and the timing window to match the CLAS event start time and the tagger hit time was 0.8 ns. In addition only tagger E-counters from 1 to 175 were used because they match the T-counters from 1 to 19 which were included in the tagger part of the trigger. Note that tagger cut is only imposed when cross section is calculated. This cut is not present in the cases of "Liberal Selection" of events described above in Sec 8.1.

10 Acceptance

10.1 Definition

In order to relate the experimental yields to the cross sections, one needs to calculate the acceptance and the efficiency of the detector. Since CLAS is a very complicated detector covering almost 4π of solid angle, it is virtually impossible to separate efficiency calculations from geometrical acceptance calculations. For this reason in this analysis we refer to acceptance corrections as a combined correction factor due to the geometry of the detector and the inefficiencies of detection and reconstruction. Our definition of acceptance is the ratio of the number of reconstructed simulated events in a invariant mass bin to the total number of simulated events for the same bin. Since the detector has a finite resolution it is possible that an event produced in one bin is reconstructed in a different bin, and therefore one would need a matrix to fully account for such bin migration effects. If the number of events created in the i-th bin is N_i and the number of reconstructed events

in j-th bin is R_j, then:

$$R_i = \sum_j M_{ij} N_j, \tag{6}$$

$$N_i = \sum_j M_{ij}^{-1} R_j, \tag{7}$$

where M_{ij} is a large $N_{bin} \times N_{bin}$ square matrix. But in order to be able to use such a method one would also need a very large number of simulated events, which is not affordable due to the slow (1.5 event/sec) speed of the detector simulation program. In addition, the determination of the inverse of such a large square matrix is known to be a very unstable procedure. But if the event generator produces realistic distributions, then one does not need the full matrix and our definition of the acceptance as a ratio would suffice. However, the remaining model-dependence of the final results should be estimated as systematic uncertainty (see Sec. 12). The tagger inefficiency is cancelled out in the normalization procedure, therefore the tagger responce is not included in the acceptance and efficiency calculations.

The acceptance corrections were applied on a bin-by-bin basis. Each bin was weighed by a factor determined from an acceptance one-dimensional histogram. This factor is defined as the ratio of number of events reconstructed in a given bin to the number of generated events:

$$A = \frac{N_{rec}}{N_{sim}}. \tag{8}$$

In this case the uncertainty of the cross section is due to statistics in the data sample and the uncertainty in the acceptance:

$$\left(\frac{\delta\sigma}{\sigma}\right)^2 = \frac{1}{N} + \frac{\delta A^2}{A^2}, \tag{9}$$

where N is the number of events in the data bin, A and δA are the acceptance and the acceptance error for that bin. In this analysis the statistical error for the acceptance δA is determined using the formula for the binomial distribution:

$$\delta A = \sqrt{\frac{A(1-A)}{N_{gen}-1}}, \tag{10}$$

where N_{gen} is the number of the Monte-Carlo (MC) events generated in an acceptance bin.

10.2 Simulations

In order to calculate the acceptance, approximately 30 million $\gamma d \to K^+K^+\Xi^-\pi^- p_s$ events were generated using a phase space event generator [22] which also has the Fermi-motion smearing incorporated in it. The output file, containing "MCTK" and "MCVX" banks from the event generator, were fed to *GSIM* [23] - a program which simulates the response of the CLAS detector. The Čerenkov counter and tagger response from GSIM were not used. The former was not yet been adequately modeled and is not used in this analysis at all. The tagger efficiency is taken into account in the photon determination procedure. The GSIM geometry was set using the standard values from the straight track analysis [24] for the drift chambers and the survey geometry for the TOF system [25] by using the *GSIM* key "RUNG=10". In order to eliminate signals from known dead channels, the GSIM Post Processor (GPP) program was used to remove signals from dead wires in the drift chambers and bad tubes in the scintillator counters. It also allows the user to smear the distance-of-closest-approach distribution in the DC and the TOF signals to match the invariant mass distributions and timing spectrum in the real data. Then the *GSIM* files were processed with the RECSIS program to reconstruct the simulated events. The executable of the reconstruction program was build with the same *Pass2v1* set of libraries which were used for processing the actual data from the EG3 running period. In the final stage the output files were analyzed to produce the acceptance histogram. The same cuts used on the experimental data were also applied to the simulated data to determine the acceptance.

The invariant mass spectrum for the $p\pi^-$, $\Lambda\pi^-$ and $\Xi^-\pi^-$ spectra from GSIM are shown in Fig. 10. The $p\pi^-$ spectrum features a peak due to $\Lambda(1116)$ which was in every simulated event. The $\Lambda\pi^-$ spectrum shows an enhancement near $M = 1.321$ `GeV` corresponding to the simulated $\Xi^-(1321)$. The $\Xi^-\pi^-$ spectrum shown here was produced with events which contained an infinitely narrow $\Phi^{--}(1862)$ state decaying into $\Xi^-\pi^-$, and the corresponding peak can be seen in Fig. 10 c. One also should note that the widths of these distributions are compatible with the data: the width for $\Lambda(1116)$ in the simulation is f~ 1.45 `MeV` versus the width from the data of ~ 1.54 `MeV`, while the GSIM width for the $\Xi^-(1321)$ is ~ 2.4 `MeV` versus ~ 2.3 `MeV` in the data by using the "conservative selection". The expected detector resolution for the $\Phi^{--}(1860)$ mass is ~ 7 MeV with a zero-width assumption in the event generator.

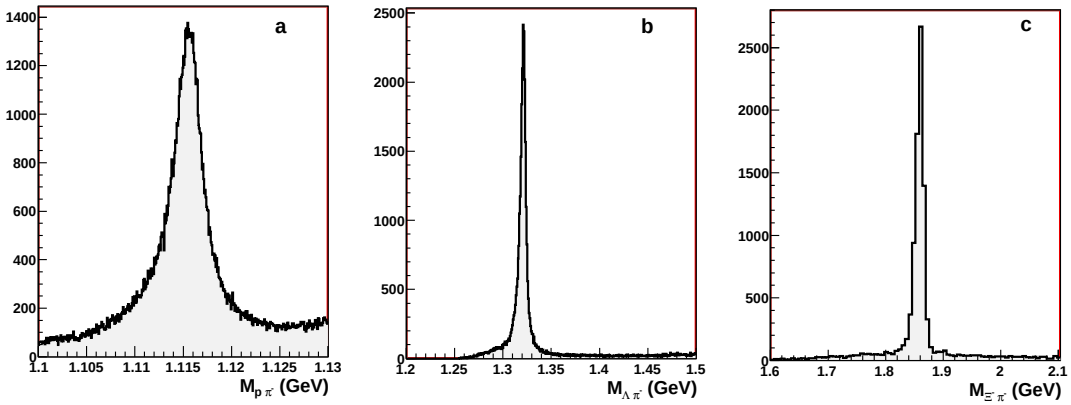

Figure 10: Invariant mass distributions from GSIM for $p\pi^-$ (a), $\Lambda\pi^-$ (b) and $\Xi^-\pi^-$ (c) systems. For all three cases the width of the distribution is due to the detector resolution.

The same cuts applied in the data were applied to the simulated events. The small differences in the widths and the peak positions were taken into account by shifting and widening/narrowing the cuts in the appropriate directions. The most significant adjustment of the cut was needed for the time difference between the pion and proton at the Λ identification stage where a 200 ps time shift was necessary, in the analysis of the simulated events. The widths of the time distributions in the simulation and the CLAS data were compatible.

The CLAS acceptance versus invariant mass of $\Xi^-\pi^-$ system is shown in Fig. 11. The acceptance is small near the threshold, slowly increasing with the invariant mass. The value of the acceptance at mass $M_{\Xi^-\pi^-} = 1.860$ GeV is $\sim 0.4\%$.

10.3 Model Dependence

Because we do not know how the cross section of the $\Phi^{--}(1862)$ photoproduction depends on the kinematics, and we integrate over all of the kinematic variables, our estimate of the CLAS acceptance may strongly depend on the choice of the distribution of the events over phase space. In order to estimate the uncertainty of the acceptance due to the model dependence we performed a study using various distribution in the event generator. The studies config-

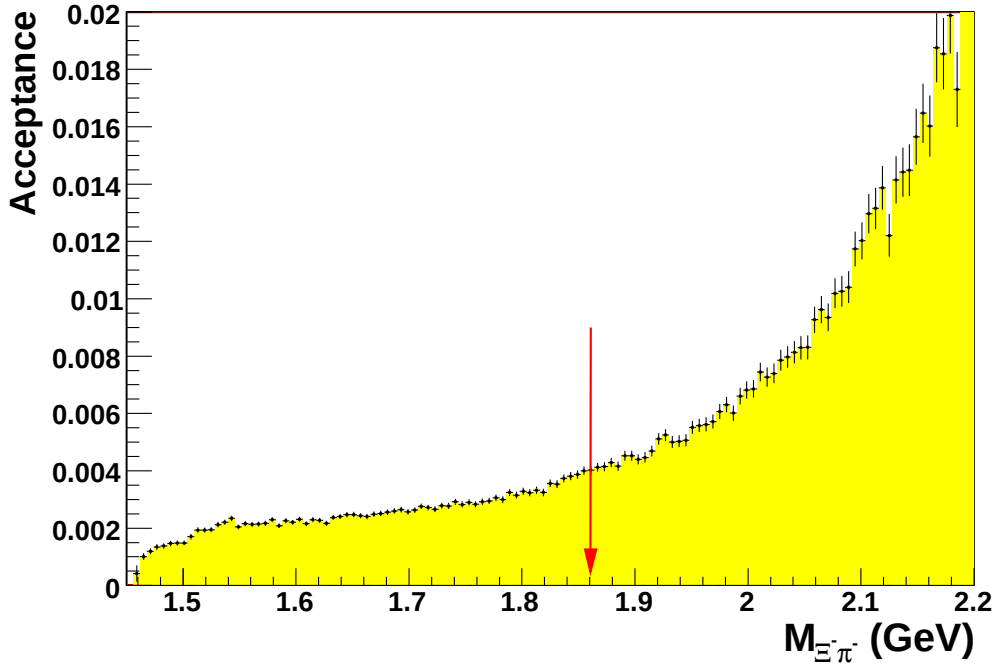

Figure 11: Acceptance of CLAS versus invariant mass of $\Xi^-\pi^-$ system determined from $\gamma d \to K^+K^+\Xi^-\pi^-p_s$ phase space simulation using GEANT-based detector simulation package GSIM. The red arrow points to the position of the peak seen by NA49 collaboration.

ID	Simulated Reaction	$\frac{\delta A}{A}$
1	$\gamma d \to K^+K^+\Xi^-\pi^- p_s$	+31 %
2	$\gamma d \to K^+\Sigma^-(2650)p_s \to K^+K^+\Phi^{--}p_s \to K^+K^+\Xi^-\pi^- p_s$	+3 %
3	$\gamma d \to K^+_f\Sigma^-(2650)p_s \to K^+_f K^+\Phi^{--}p_s \to K^+_f K^+\Xi^-\pi^- p_s$	-10 %
4	$\gamma d \to K^+K^+\Phi^{--}p_s \to K^+K^+\Xi^-\pi^- p_s$	-23 %

Table 1: Event configurations used for model dependence studies.

urations are give in Table 1. The events were simulated using *fsgen* package for simulating events according to flat phase space. The reaction # 1 in Table 1 is a four-body phase-space uniform distribution complemented with a spectator proton with a Fermi momentum smearing. For the process in row #2 a hypothetical $\Sigma(2650)$ was implemented in the code, that decayed into $K^+\Phi^{--}$ with total width of 35 MeV. The $\Phi^{--}(1862)$ was simulated as a particle with a infinitely narrow mass $M_\Phi = 1.862$ GeV decaying only through $\Xi^-\pi^-$ channel. The reactions #2 and #4 are simulated according to two- and three-body phase space accordingly, with a spectator proton with Fermi momentum. The process in row #3 in Table 1 is simulated according to two-body phase-space but with additional t-slope distribution for the K^+, taken with $b = 8$ GeV^{-2} t-slope paramater. Such a large value of b is chosen to simulate the extreme case of forward peaking angular distribution. Thus, the flat phase space is supposed to give us the estimate of the acceptance for the s-channel processes, while including a steep t-dependence would allow us to consider the processes going through the t-channel exchanges.

The third column in Table 1 shows the deviation of the estimated CLAS acceptance for given process with respect to the average acceptance. For processes in rows from #2 to #3 the acceptance is estimated at a fixed mass $M_{\Xi^-\pi^-} = 1.862$ GeV since the process explicitly includes the $\Phi^{--}(1862)$ decay. For the case of the four-body phase space in raw #1 the acceptance is also estimated near $M_{\Xi^-\pi^-} = 1.862$ GeV. From this table we assign a relative uncertainty of $\frac{\sigma^{sys}_A}{A} \sim 25\%$ due to model dependence. This is by far the largest source of uncertainty in the determination of the cross sections or its upper limits.

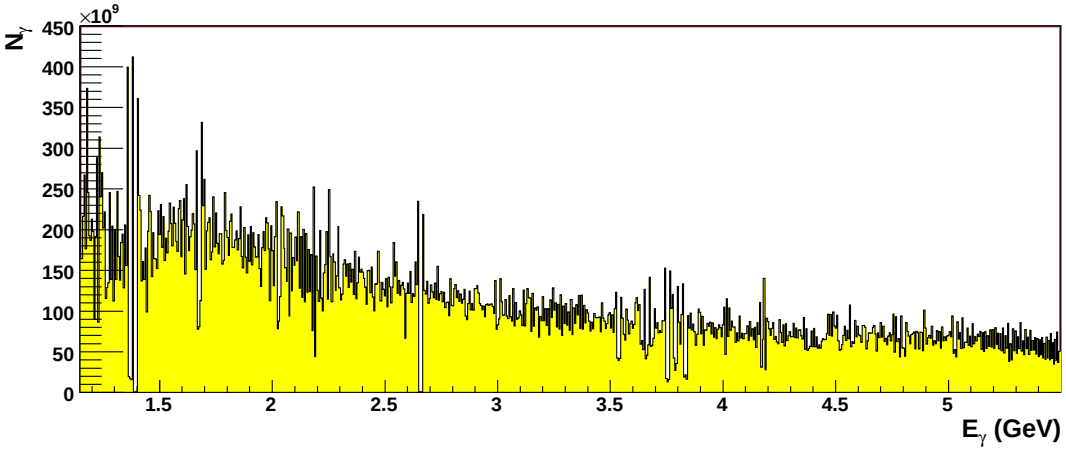

Figure 12: Number of photons per energy bin versus corresponding photon energy as determined by *gflux* package.

11 Normalization

In order to extract the absolute cross sections or the upper limit for the cross section one needs to determine the intergated luminosity corresponding to the analyzed data sample. The integrated luminosity is the product of the photon flux passing through the target and the number of the elementary targets per unit surface:

$$L = \frac{N_\gamma \times N_{^2H}}{S}, \tag{11}$$

where N_γ is the number of photons, $N_{^2H}$ is the number of deuteron targets, and S is the effective target surface. The total number of photons per tagger energy bin is determined using *gflux* package [26]. The total number of deuteron targets per unit surface is estimated as:

$$\frac{N_{^2H}}{S} = \frac{2\rho_{^2H} L_T N_A}{M_{^2H}}, \tag{12}$$

where $\rho_{^2H}$ is the density of liquid deuterium from Ref. [19], L_T is the target length equal to 40 cm, N_A is the Avogadro number[19], $M_{^2H}$ is the molar mass of ^2H and is equal to 4.02 $\frac{g}{mol}$. Factor of two is present since a deuterium molecule contains two deuteron targets.

The number of photons reported by the *gflux* is already corrected for the detector livetime, which means that the number of events in the data sample does not need to be corrected for the deadtime of the detector. The tagger efficiency in the event reconstruction and *gflux* cancel out because the photon reconstruction algorithm in the two procedures is the same. Fig. 12 shows the number of the photons per energy bin corresponding to the data sample which was analyzed in this work. This analysis uses only the portion of the tagger corresponding to the energy range 4.55 GeV $< E_\gamma <$ 5.5 GeV. The typical uncertainties reported by *gflux* package for a single energy bin is on the order of $\sim 2\%$.

12 Systematics

The final spectrum for the invariant mass was studied for various values of the cut parameters for Λ, Ξ and π^- selection. These variations did not result in the qualitative change of the invariant spectrum of the invariant mass of $\Lambda\pi^-\pi^-$ or $\Xi^-\pi^-$ spectrum. In addition three independent parallel analysis, one of which included a kinematical fitting of the masses and vertexes of $\Lambda(1116)$ and $\Xi^-(1321)$, lead did not produce any statistically enhancements near mass $M = 1.860$ GeV.

The dominant contribution to the photoproduction cross section systematic uncertainty is from the model dependence of the estimated acceptance value, and our simulation suggest $\sim$ 25% relative uncertainty for the acceptance. All other systematic uncertainties in CLAS are typically under 10%, and therefore are neglected in this analysis, keeping in mind that the statisticall error bars for the raw data points are on the order of $\sim 20\%$.

During the offline analysis we noticed that the yields for four-track events in the three sector trigger were reduced by $\sim 20\%$ when the start counter was put in coincidence with the tagger Master OR signal before it was sent to the asynchronous trigger input of the CLAS trigger superwiser. This effect was accounted for by scaling the yields up by 16%, after taking into account the amount of time such a configuration of the trigger was used. An additional systematic uncertainty of 10% was assign to the normalization.

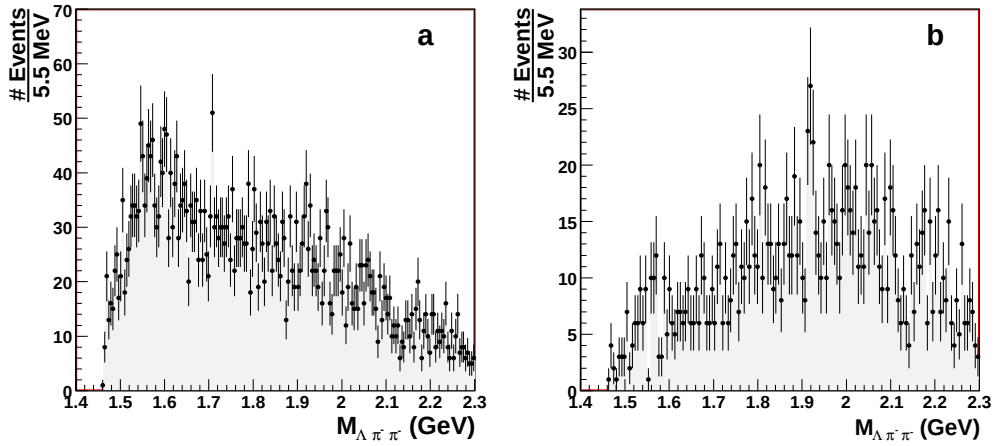

Figure 13: Invariant mass spectrum of $\Lambda\pi^-\pi^-$ system with "liberal selection" and $c\tau > 1.5$ cm with (a) and without (b) requirement for an extra K^+. There is no statistically significant enhancement near mass $M = 1.860$ GeV.

13 Invariant mass spectrum for $\Lambda\pi^-\pi^-$ system

Once the Λ is identified we select only the events which contain at least two negative pions. For these events we construct the invariant mass of $\Lambda\pi^-$ either using the "Liberal selection" or the "Conservative selection" methods. The mass spectrum using "liberal" method with $c\tau > 1.5$ cm cut shown on on Fig. 6 a exhibits sharper peak than one in the Fig. 7 containing all $\Lambda\pi^-$ combinations with fiducial cuts, good run selection and photon matching in the tagger, but no $c\tau$ cut ("conservative selection").

By applying a mass cut around the Ξ^--peak in Fig. 6 a we can construct the invariant mass of $\Lambda\pi^-\pi^-$ system, shown in Fig. 13. The spectrum does not exhibit any statistically significant enhancement near $M_{\Lambda\pi\pi} = 1.860$GeV. The spectrum contains $\Xi^-\pi^-$ events as well as non-cascade events. Therefore it is desirable to subtract the contribution of the non-cascade events to the $\Lambda\pi^-\pi^-$ mass spectrum, thus obtaining the $\Xi^-\pi^-$ invariant mass spectrum.

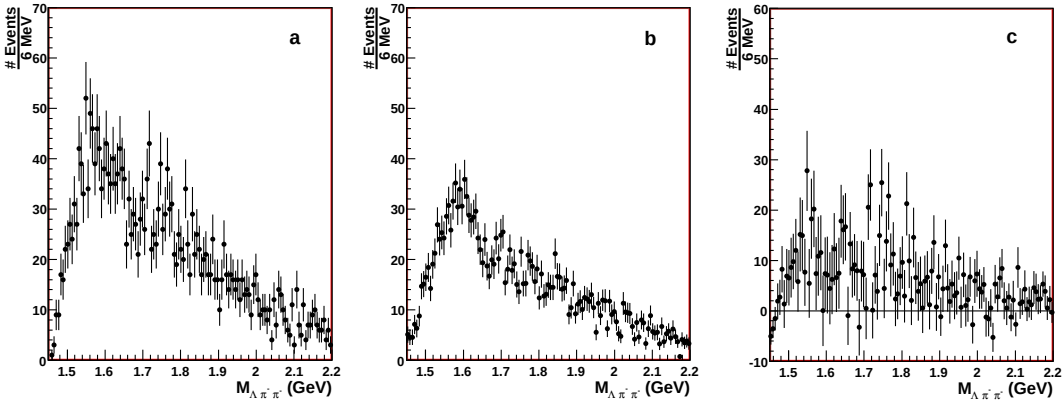

Figure 14: Invariant mass distribution of $\Lambda\pi^-\pi^-$ system with "conservative selection" with $c\tau > 0$ cm for $\Lambda\pi^-\pi^-$ events. The spectrum for all events under the Ξ^- peak are shown in panel (a), from left and right sidebands normalized to the background under the peak in panel (b), and the sideband subtracted spectrum in panel c.

14 Invariant mass spectrum for $\Xi^-\pi^-$ system

The spectrum of interest for this analysis is of the invariant mass of $\Xi^-\pi^-$ system, which we obtain from the data sample with "Conservative Selection" of events. There are at least two different ways to obtain this spectrum. First method is to select events containing $\Lambda\pi^-\pi^-$ system, put a tight cut around $\Xi(1321)$ peak, and from the $\Lambda\pi^-\pi^-$ mass spectrum of the selected events subtract the backround evaluate using sideband subtraction method. Alternatively, one can first bin all events in $\Lambda\pi^-\pi^-$ mass, and for each bin perform a fit in $\Lambda\pi^-$ to extract the $\Xi^-\pi^-$ yields.

14.1 Sideband Subtraction

We consider this method our main method of obtaining $\Xi^-\pi^-$ mass spectrum. Again, we put a cut around $\Xi(1321)$ peak and combine $\Lambda\pi^-$ with another π^-, and plot the invariant mass of $\Lambda\pi^-\pi^-$ system, shown on Fig. 14 a. To account for the background non-cascade background we select sidebands from the left and the right sides of the $\Xi^-(3121)$ peak and use those events to subtract the background contribution in the $\Lambda\pi^-\pi^-$ mass spectrum. The $\Lambda\pi^-\pi^-$ mass

spectrum of the events from the two sidebands, Fig. 14 b, is normalized to the number of background events underneath the cascade peak. The subtracted mass dependence is shown on Fig. 14 c. There is no statistically significant enhancement near mass $M_{\Xi\pi} = 1.860\texttt{GeV}$.

This procedure was performed for different cuts on $c\tau[\Xi]$ to check for presence of any statistically significant enhancement near 1.862 GeV in the sideband-subtracted spectrum. None of the plots for $\Xi^-\pi^-$ invariant mass exhibited any peaking near that mass range.

14.2 Cross-check with Fitting method

To cross check the sidebandband subtraction method we also extracted the yields of $\Xi^-\pi^-$ events in each $\Lambda\pi^-\pi^-$ mass bin by fitting the $\Lambda\pi^-$ mass and $c\tau[\Xi]$ distributions. Instead of fitting one dimensional histograms with a fixed $c\tau[\Xi]$ cut we performed a two-dimensional fit with one axis defined by $\Lambda\pi^-$ mass, and the other axis by $c\tau[\Xi]$. The model for the fit assumed Gaussian distribution for the $c\tau[\Xi]$ and Breit-Wigner for invariant mass for events from $\Sigma^-(1385)$ decays. The events from $\Xi^-(1321)$ decays are assumed to be distributed according to a convolution of a Gaussian and exponential in $c\tau[\Xi]$, and to a Gaussian in invariant mass. The "unknown" background is parametrized in form of two polynomials in $\Lambda\pi^-$ mass terms: first term is Gaussian in $c\tau[\Xi]$, the second term behaves as a convolution of a Gaussian and exponential. The fitting procedure uses maximum likelihood method [27] because of the limited number of events in each $\Lambda\pi^-\pi^-$ mass bin. The comparison of the results from the sideband subtracted method and fitting method is shown in Fig. 15. The bin sizes in this plot are chosen wider than in Fig. 14 c, $\Delta M = 20$ MeV because we need a reasonable population in each $\Lambda\pi^-\pi^-$ mass bin to perform a fit. One can see that the two methods provide consistent results. Because the required binning for this procedure was too crude we did not use this method to obtain our final results.

15 Upper Limits

In order to extract the upper limits for the number of events and the photoproduction cross sections we utilized statistical analysis method similar to one describe in Ref. [28]. The cases described in Ref. [28] had already been implemented in the ROOT framework [18]. This method allows us to

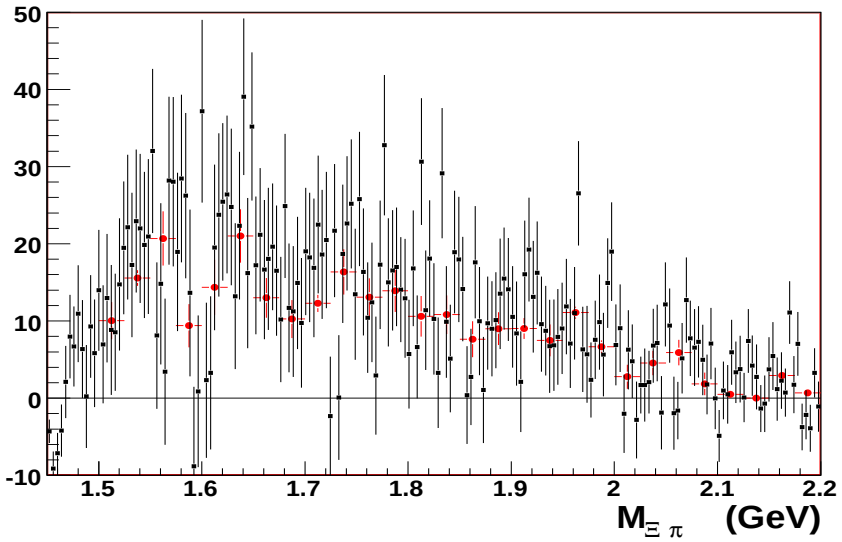

Figure 15: Comparison of the results for $\Xi^-\pi^-$ yields versus the invariant mass of the system. The red marker shows the result of the fitting method, while the black markers show the result of the sideband subtraction method. The yields from the sideband subtraction method is scaled by the ratio of the bin widths.

estimate the confidence belt for predetermined confidence level for models containing various nuisance parameters with their uncertainties. In this case these parameters are the background and acceptance/efficiency. For specified number of total observed events, estimated number of background events, the error for the estimated number of background events, acceptance/efficiency of the detector, and the uncertainty for the acceptance/efficiency, this method gives the corresponding confidence belt at a given confidence level (CL). As you will see from the sections below, we estimate that the upper limit for photoproduction cross section for $\Phi^{--} \rightarrow \Xi^{-}\pi^{-}$ in the energy range $4.5\ \texttt{GeV} < E_{\gamma} < 5.5\ \texttt{GeV}$ in a mass window of 20 MeV at 90% confidence level is ~ 200 pb.

15.1 Methods to estimate the upper limits

To estimate the upper limit we scan through the bins of the mass-dependent histogram. For each bin in the spectrum of the invariant mass of the $\Lambda\pi^{-}\pi^{-}$ system we select a 20 MeV wide window centered at that bin, and determine the upper limit of the excess events over the background. To estimate the number of background events we fit the histogram in Fig. 13 or Fig. 14 c with a smooth polynomial plus a Gaussian. The center of the Gaussian is fixed at the center of the bin, while the width of the Gaussian distribution is fixed at 7 MeV. Our studies show that the result practically does not depend on the choice of the width of the Gaussian. In fact, we get similar results even if we only use a polynomial function without Gaussian to estimate the background. The procedure to determine the acceptance/efficiency of the detection and reconstruction in CLAS is described in Sec. 10. In order to test the upper limit extraction procedure we performed a cross check with three methods. Our main method for obtaining the upper limits is the Rolke method with Gaussian signal described in Sec. 15.1.2. For clarity we start by describing the Rolke method with Poisson distribution for total number of events from Ref. [28].

15.1.1 Rolke Method with Poisson Statistics

The first method is one of the models described in details in Ref. [28]. Working with the unsubtracted histogram in Fig. 13, using the total number of events in the window, the background, the acceptance and their uncertainties we can obtain the upper limit for the number of events using a Poisson

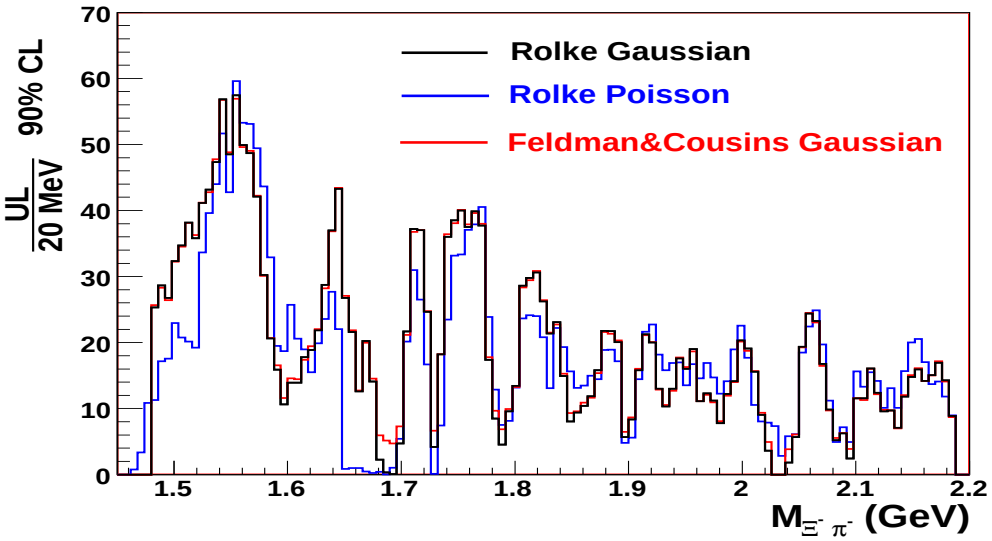

Figure 16: Upper limits for the number of events in 20 MeV window at 90% confidence level versus the mass of $\Lambda\pi^-\pi^-$ system. The black line shows the upper limit from sideband-subtracted histogram using Rolke method with Gaussian signal. The red line shows the upper limits from sideband-subtracted histogram using Feldman-Cousins method. The blue line shows the upper limits from unsubtracted histogram using Rolke method with Poisson model for the total number of events in the window.

model for the total number of events with Gaussian background and acceptance distributions using standart ROOT method. But for comparison here we ignore the acceptance and background uncertainties and assume 100% acceptance/efficiency. The reason for this is that one of the three methods described below is not well suited to handle acceptance and background uncertainties. The dependence of the upper limit at 90% confidence level for the number of the Φ^{--} events versus invariant mass of $\Lambda\pi^-\pi^-$ system with this method is shown with blue line on Fig. 16.

15.1.2 Rolke Method with Gaussian Statistics

The second method uses the sideband-subtracted histogram in Fig. 14 c. In this case the number of events is distributed according to Gaussian distribution because after subtracting the non-cascade background contribution the number of events and its variance are not related by $D(N) = \frac{1}{N}$ as it is in the case of binomial distribution. Here, the model for the excess of the events above the background is modeled by a Gaussian, limited by $\mu \geq 0$ condition since the cross section cannot be negative even if the number of observed events is less than the expected background. The rest of the procedure is similar to the method described in Ref. [28]. Again, for comparison here we ignore the acceptance and background uncertainties and assume 100% acceptance/efficiency. The dependence of the upper limit at 90% confidence level for the number of Φ^{--} events versus invariant mass of $\Xi^-\pi^-$ system from the sideband-subtracted histogram is shown with black line on Fig. 16.

15.1.3 Feldman-Cousins method

In addition to the Rolke method [28] we performed a cross-check of our upper limit results for the total number of events using Feldman-Cousins method [29] used in previous CLAS pentaquark analyses. We used the Feldman-Cousins method for the case of the Gaussian distribution for the signal with boundary limit on expectation value $\mu \geq 0$ as described in Ref. [30]. A comparison of the three methods is shown in Fig. 16, where Feldman-Cousins method is represented by the red curve. As in the two previous cases the acceptance/efficiency is set to be 1, and zero background and acceptance uncertainty is assumed. Overall, the three methods are in good agreement, but there is relatively small discrepancies between the unsubtracted and subtracted methods in the mass range under $M < 1.75$ `GeV`. These differences

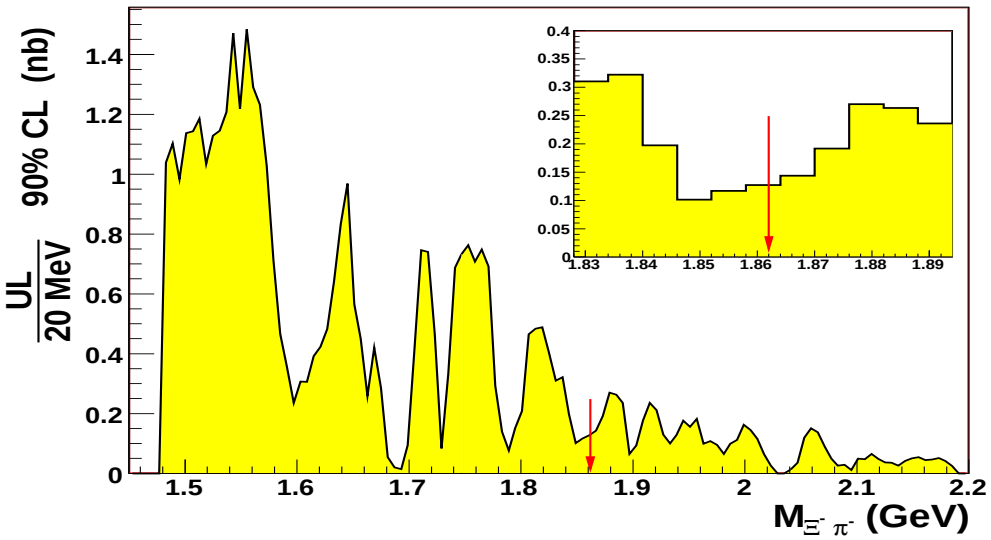

Figure 17: Upper limits for the photoproduction cross section in 20 MeV window at 90% confidence level versus the mass of $\Xi^-\pi^-$ system. The red arrow shows where the position of the enhancement from the NA49 experiment.

can be explained by the fact that subtraction of sidebands introduces additional statistical uncertainty, therefore the upper limit estimates do not have to be identical before and after subtraction.

15.2 Upper limits for cross sections

In order to obtain the upper limit for the photoproduction cross sections for a mass window of 20 MeV we have to divide the number of events by the integrated luminosity. The uncertainty in the luminosity determination is negligible, on the order of $\sim 2\%$, compared to the model dependence of the acceptance calculation described in Sec. 10. The procedure for determining the luminosity is described in Sec. 11. Here we apply our method with Gaussian model for the excess of events using the sideband-subtracted histogram in Fig. 14 c. This time we use the real estimated acceptance and the realistic uncertainties in the acceptance and the background. Fig. 17 shows the upper limit for the cross section using the sideband-subtracted histogram versus invariant mass of $\Xi^-\pi^-$. The events in these plots were selected to have a matching photon in the energy range 4.55 GeV$< E_\gamma <$ 5.5 GeV. The upper

limit for the cross section in the mass range of 1.83 GeV$< M_{\Lambda\pi\pi} <$ 1.89 GeV at these photon energies is $\sim$ 200 pb.

16 Conclusions

We analyzed the entire EG3 data set to look for the $\Phi^{--}(1862)$ pentaquark candidate in the $\Phi^{--}(1862) \to \Xi^-\pi^-$ decay channel. The raw event spectrum does not show any statistically significant enhancement near the mass $M_{\Lambda\pi^-\pi^-} = 1.862$ GeV, neither does the sideband-subtracted spectrum. The upper limit for photoproduction cross section versus invariant mass of the $\Xi^-\pi^-$ was obtained using method similar to one described in Ref. [28]. On average the upper limit for the cross sections for Φ^{--} photoproduction near the threshold with subsequent decay $\Phi^{--} \to \Xi^-\pi^-$ at 90% confidence level for 20 MeV mass window in the energy range of 1.83 GeV$< M_{\Lambda\pi\pi} <$ 1.89 GeV is $\sim$ 200 pb. This is an order of magnitude improvement over the previously estimated upper limit from HERMES collaboration of $\sim$ 2 `nb` [4].

A Appendix

A.1 Good Runs

45552	45553	45554	45555	45556	45557	45558	45563	45566	45568
45569	45570	45571	45572	45576	45577	45578	45579	45580	45581
45582	45598	45599	45600	45601	45602	45603	45605	45606	45607
45608	45609	45612	45613	45614	45621	45622	45623	45624	45625
45626	45627	45804	45807	45808	45809	45810	45811	45812	45814
45815	45816	45817	45818	45847	45848	45851	45852	45860	45862
45863	45864	45866	45868	45869	45870	45872	45873	45874	45876
45891	45893	45894	45895	45896	45897	45902	45903	45904	45905
45906	45907	45911	45912	45913	45914	45916	45917	45918	45919
45920	45921	45922	45923	45924	45925	45926	45927	45928	45929
45930	45931	45932	45933	45934	45935	45936	45937	45938	45939
45942	45943	45944	45945	45946	45947	45948	45976	45977	45978
45981	45983	45984	45985	45986	45987	45988	45993	45995	45996
46000	46001	46002	46003	46004	46005	46009	46011	46012	46013
46014	46015	46016	46017	46018	46019	46020	46021	46022	46023
46024	46025	46028	46029	46030	46035	46036	46037	46038	46046
46047	46057	46058	46062	46063	46064	46065	46066	46069	46071
46072	46073	46074	46077	46078	46085	46086	46087	46088	46089
46093	46094	46096	46097	46098	46099	46100	46101	46104	46113

Table 2: Table of the CLAS runs used in this analysis.

References

[1] D. Diakonov, V. Petrov, and M. Polyakov. Exotic Anti-Decuplet of Baryons: Prediction from Chiral Solitons. *Z. Phys. A*, 359:305, 1997. [hep-ph/9703373].

[2] C. Alt et al. (NA49 Collaboration). Observation of an Exotic S = -2, Q = -2 Baryon Resonance in Proton-Proton Collisions at the CERN SPS. *Phys. Rev. Lett.*, 92:042003, 2004. [hep-ex/0310014].

[3] M. I. Adamovich et al. Search for the exotic xgr –(1860) resonance in 340 gev c sigma –nucleus interactions. *Phys. Rev.*, C70:022201, 2004.

[4] A. Airapetian et al. Search for an exotic s = -2, q = -2 baryon resonance at a mass near 1862-mev in quasi-real photoproduction. *Phys. Rev.*, D71:032004, 2005.

[5] S. Chekanov et al. Search for pentaquarks decaying to xi pi in deep inelastic scattering at hera. *Phys. Lett.*, B610:212–224, 2005.

[6] E. S. Ageev et al. Search for the phi(1860) pentaquark at compass. *Eur. Phys. J.*, C41:469–474, 2005.

[7] K. T. Knopfle, M. Zavertyaev, and T. Zivko. Search for theta+ and xi(3/2)– pentaquarks in hera-b. *J. Phys.*, G30:S1363–S1366, 2004.

[8] B. Aubert et al. Search for strange-pentaquark production in e^+e^- annihilation at $\sqrt{s} = 10.58$ gev. *Phys. Rev. Lett.*, 95:042002, 2005.

[9] Kevin Stenson. Pentaquark searches at focus. *Int. J. Mod. Phys.*, A20:3745–3748, 2005.

[10] A. Abulencia et al. Search for exotic s = -2 baryons in p anti-p collisions at s**(1/2) = 1.96-tev. *Phys. Rev.*, D75:032003, 2007.

[11] S. Schael et al. Search for pentaquark states in z decays. *Phys. Lett.*, B599:1–16, 2004.

[12] P. Achard et al. Study of inclusive strange-baryon production and search for pentaquarks in two-photon collisions at lep. *Eur. Phys. J.*, C49:395–410, 2007.

[13] A. Aktas et al. Search for baryonic resonances decaying to xi pi in deep-inelastic scattering at hera. 0400.

[14] B. A. Mecking et al. The cebaf large acceptance spectrometer (clas). *Nucl. Instrum. Meth.*, A503:513–553, 2003.

[15] D. Diakonov and V. Petrov. Where are the missing members of the baryon antidecuplet? *Phys. Rev. D*, 69:094011, 2004. [hep-ph/0310212].

[16] R. Gothe, H. Holtrop, E.S. Smith, and S. Stepanyan. Spokespersons for Search for "Exotic Cascades with CLAS Using an Untagged Virtual Photon Beam". JLab Experiment E-04-010, 2004.

[17] E. Blobel. The bos system for clas software. CLAS-NOTE 2007-016, 1995.

[18] R. Brun and F. Rademakers. Root: An object oriented data analysis framework. *Nucl. Instrum. Meth.*, A389:81–86, 1997.

[19] W. M. Yao et al. Review of particle physics. *J. Phys.*, G33:1–1232, 2006.

[20] E. Pasyuk. Energy loss corrections for charged particles in clas. CLAS-NOTE 2007-016, 2007.

[21] Paul Mattione. Kinematic fitting of detached vertices. JLAB-PHY-07-643, May 2007.

[22] Stepan Stepanyan. Fsgen phase space generator. Private Communications.

[23] Maurik Holtrop. Clas geant simulation. www.physics.unh.edu/maurik/gsim_info.shtml.

[24] Robert Feuerbach et al. Drift chamber alignment. CLAS-NOTE 1998-002, 1998.

[25] G. Mutchler, S. Taylor, and E. Smith. Clas tof scintillator positions. CLAS-NOTE 1998-008, 1998.

[26] J. Ball and E. Pasyuk. Photon flux determination through sampling of out-of-time hits with the hall b photon tagger. CLAS-NOTE 2005-002, 2005.

[27] G. Cowan. *Statistical Data Analysis*, chapter 6. Oxford Science Publication, 1998.

[28] Wolfgang A. Rolke, Angel M. Lopez, and Jan Conrad. Confidence intervals with frequentist treatment of statistical and systematic uncertainties. *Nucl. Instrum. Meth.*, A551:493–503, 2005.

[29] Gary J. Feldman and Robert D. Cousins. A unified approach to the classical statistical analysis of small signals. *Phys. Rev.*, D57:3873–3889, 1998.

[30] Elton Smith. Feldman-cousins method for gaussian statistics. CLAS-NOTE 2007-019, 2008.